LETTER

A Rapidly Star-forming Galaxy 680 Million Years After the Big Bang at z=7.51

S. L. Finkelstein[1], C. Papovich[2], M. Dickinson[3], M. Song[1], V. Tilvi[2], A. M. Koekemoer[4], K. D. Finkelstein[1], B. Mobasher[5], H. C. Ferguson[4], M. Giavalisco[6], N. Reddy[5], M. L. N. Ashby[7], A. Dekel[8], G. G. Fazio[7], A. Fontana[9], N. A. Grogin[4], J.-S. Huang[7], D. Kocevski[10], M. Rafelski[11], B. J. Weiner[12] & S. P. Willner[7]

There are five spectroscopically confirmed z > 7 galaxies, all confirmed via Lymanα emission at z=7.008, 7.045, 7.109, 7.213 and 7.215.[1-4] The small fraction of confirmed galaxies may indicate that the neutral fraction in the intergalactic medium (IGM) rises quickly at $z > 6.5$, as Lymanα is resonantly scattered by neutral gas.[3,5-8]. However, the small samples and limited depth of previous observations makes these conclusions tentative. Here we report the results of a deep near-infrared spectroscopic survey of 43 $z > 6.5$ galaxies. We detect only a single galaxy, confirming that some process is making Lymanα difficult to detect. We conclude that the detected emission line at 1.0343 μm is likely to be Lymanα emission, placing this galaxy at a redshift z = 7.51, an epoch 680 million years after the Big Bang. This galaxy's colors are consistent with significant metal content, implying that galaxies become enriched rapidly. We measure a surprisingly high star formation rate of 330 M$_\odot$ yr^{-1}, more than a factor of 100 greater than seen in the Milky Way. Such a galaxy is unexpected in a survey of our size[9], thus the early universe may harbor more intense sites of star-formation than expected.

We obtained near-infrared (near-IR) spectroscopy of galaxies originally discovered in the Cosmic Assembly Near-infrared Deep Extragalactic Legacy Survey (CANDELS)[10,11] with the newly-commissioned near-infrared spectrograph MOSFIRE[12] on the Keck I 10 meter telescope. From a parent sample of over 100 galaxy candidates at $z > 7$ selected via their *HST* colors through the photometric redshift technique[13-16], we observed 43 candidate high-redshift galaxies over two MOSFIRE pointings with exposure times of 5.6 and 4.5 hr, respectively. Our observations covered Lyα emission at redshifts of 7.0 – 8.2. We visually inspected the reduced data at the expected slit positions for our 43 observed sources, and found plausible emission lines in seven objects, with only one line detected at $>5\sigma$ significance. The detected emission line is at a wavelength of 1.0343μm with an integrated signal-to-noise (S/N) of 7.8 (Figure 1), and comes from the object designated z8_GND_5296 in our sample (RA=12:36:37.90; Dec=62:18:08.5 J2000). Based on the arguments outlined below (and discussed extensively in the supplementary material), we identify this line as the Lyα transition of hydrogen at a line-peak redshift of $z = 7.5078 \pm 0.0004$; consistent with our photometric redshift 68% confidence range of $7.5 < z < 7.9$ for z8_GND_5296.

As expected for a galaxy at $z = 7.51$, z8_GND_5296 is completely undetected in the *HST* optical bands, including an extremely deep 0.8 μm image (Figure 2). The galaxy is bright in the *HST* near-IR bands, becoming brighter with increasing wavelength, implying that the Lyman break lies near 1 μm, and that the galaxy has a moderately red rest-frame UV color. The galaxy is well-detected in both *Spitzer*/IRAC bands, and is much brighter at 4.5 μm than at 3.6 μm. The strong break at 1 μm restricts the observed emission line to be either Lyα at $z = 7.51$ (near the Lyman break) or [O II] $\lambda\lambda3726,3729$ (a doublet) at $z = 1.78$ (near the rest-frame Balmer/4000 Å break). We investigate these two possibilities by comparing our observed photometry to a suite of stellar population models at both redshifts (Figure 3). A much better fit to the data is obtained when using models at $z = 7.51$ than at $z = 1.78$, supporting our identification of the emission line as Lyα. Specifically, the model at $z = 1.78$ would result in $>4\sigma$ significant flux in the 0.8 μm image, as well as a near-zero IRAC color, both of which are not seen. Additionally, the $z = 1.78$ model requires an aging stellar population with no active star formation, which would have insignificant [O II] emission. In the Supplementary Information, we discuss a number of tests performed to discern between the Lyα and [O˙II] hypotheses. In summary, although we cannot robustly measure the line asymmetry due to the nearby sky residual, the SED fitting results, as well as the lack of a detected second line in the [O II] doublet, lead us to conclude that the emission line is in fact Lyα at $z = 7.51$.

This galaxy is very bright in the rest-frame UV and optical, with an apparent magnitude of m$_{F160W}$ = 25.6 and a derived stellar mass of $1.0^{+0.2}_{-0.1} \times 10^9$ M$_\odot$. The blue $H - [3.6]$ color suggests that the moderately red UV color ($J - H = 0.1$ mag) is due to dust attenuation rather than the intrinsic red color of an old stellar population. The presence of dust extinction leads to a higher inferred UV luminosity. To derive the intrinsic star-formation rate (SFR) for this galaxy, we measure a time-averaged SFR from the best-fitting stellar population models to find SFR = 330^{+710}_{-10} M$_\odot$ yr^{-1}. The very red $[3.6] - [4.5]$ color at $z = 7.51$ can only be due to strong [O III] $\lambda5007$ line emission in the 4.5 μm band; indeed, the SED fitting implies an [O III] $\lambda5007$ rest-frame equivalent width (EW) of 560 – 640 Å (68% confidence), with a line flux of 5.3×10^{-17} erg s^{-1} cm^{-2}. This very high [O III] EW can constrain the abundance of metals in this galaxy, as highly enriched stars do not produce hard enough ionizing spectra, while very low metallicity systems do not have enough oxygen to produce strong emission lines. Of the metallicities available in our models (0.02, 0.2, 0.4 and 1.0 × solar), only models with a metal abundance of about 20–40% of Solar have [O III] EWs >300 Å. Thus, even at such early times, it was possible to form a moderately chemically enriched galaxy. However, due to discreteness of the model metallicities, further analysis is needed to make more quantitative conclusions on the metallicity, particularly on the lower limit. We note that at $z = 7.51$ [O II] is in the

[1] The University of Texas at Austin, 2515 Speedway, Stop C1400, Austin, TX 78712, USA [2] Texas A&M University, 4242 TAMU, College Station, TX 78743, USA [3] National Optical Astronomy Observatory, Tucson, AZ 85719, USA [4] Space Telescope Science Institute, 3700 San Martin Dr., Baltimore, MD, 21218, USA [5] University of California, Riverside, CA 92521, USA [6] University of Massachusetts, Amherst, MA 01003, USA [7] Harvard-Smithsonian Center for Astrophysics, 60 Garden St., Cambridge, MA 02138, USA [8] Racah Institute of Physics, The Hebrew University, Jerusalem 91904, Israel [9] INAF-Osservatorio di Roma,II-00040, Monteporzio, Italy [10] University of Kentucky, Lexington, KY, 40506, USA [11] Infrared Processing and Analysis Center, MS 100-22, Caltech, Pasadena, CA 91125 [12] Steward Observatory, University of Arizona, 933 N. Cherry Ave, Tucson, AZ 85721
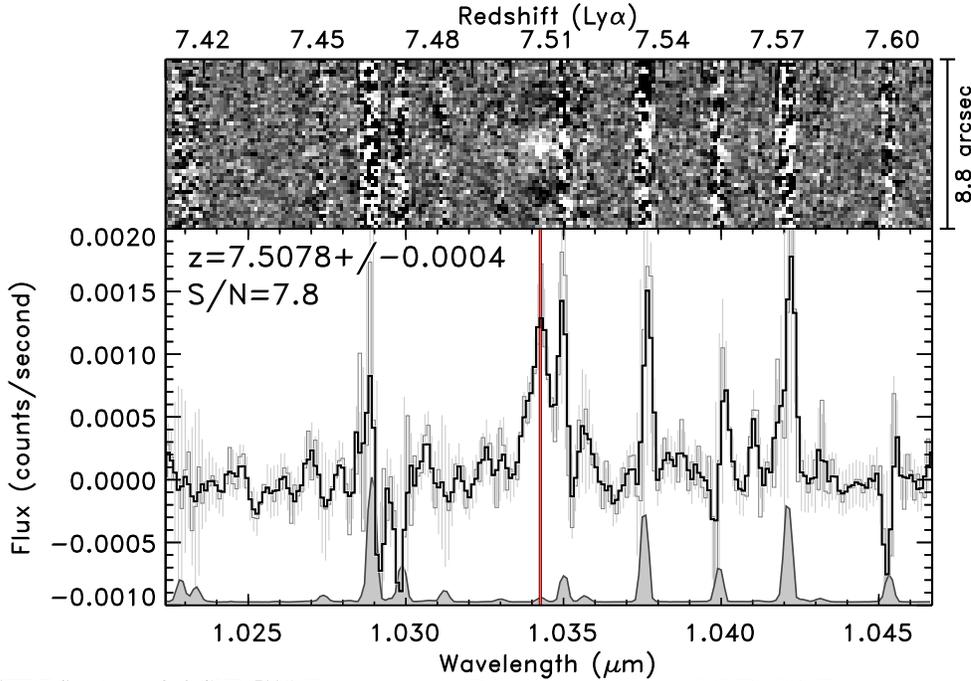
Figure 1 | MOSFIRE Spectrum of z8_GND_5296. The observed near-IR spectrum of the galaxy z8_GND_5296. The top panel shows the reduced two-dimensional spectrum, and an emission line is clearly seen as a positive signal in the center, with the negative signals above and below a result of our dithering pattern in the spatial direction along the slit; this is a pattern only exhibited for real objects. The bottom panel shows our extracted one-dimensional spectrum (smoothed to the spectral resolution in black; un-smoothed in gray). The sky spectrum is shown as the filled gray curve, with the scale reduced greatly compared to that of the data. The line is clearly detected in separate reductions of the first and second halves of the data with S/N of 6.4 and 5.2, respectively. The line has a full-width at half-maximum (FWHM) of 7.7 Å, and is clearly resolved compared to nearby sky emission lines, which have FWHM = 2.7 Å. The red line denotes the peak flux of the detected emission line, which corresponds to a redshifted Lyα line at 7.51. All other strongly positive or negative features are subtraction residuals due to strong night sky emission. Although the line appears symmetric, there is a sky line residual just to the red of our detected emission line, which makes a measurement of our line's asymmetry difficult.
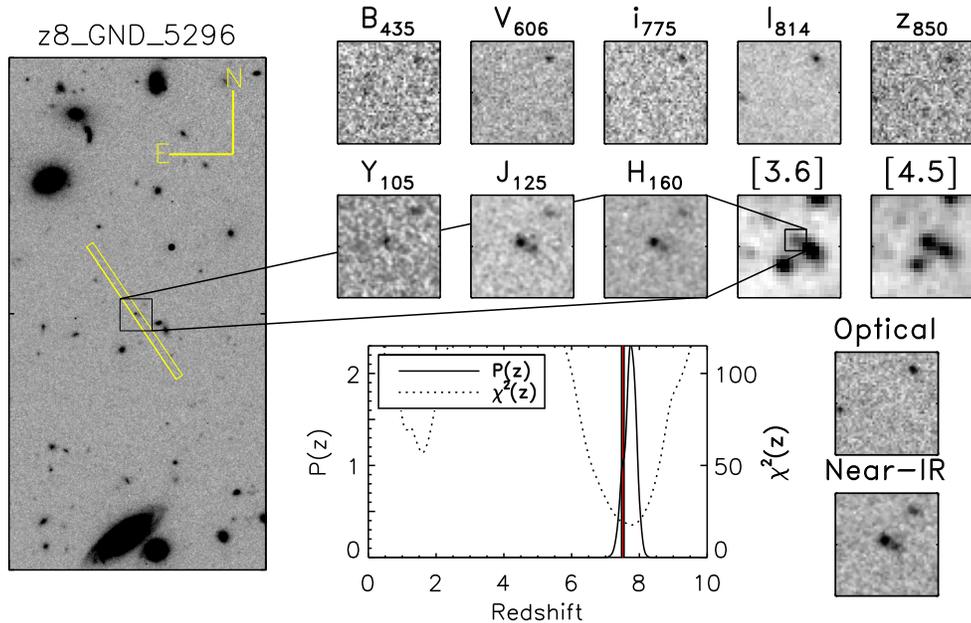
Figure 2 | Images of z8_GND_5296. Large image: A portion of the CANDELS/GOODS-N field, shown in the F160W filter (centered at 1.6μm), around z8_GND_5296. CANDELS provides the largest survey volume in the distant universe deep enough to find $z > 7$ galaxies. The $15'' \times 0.7''$ slit is shown as the yellow rectangle. Small images: Cutouts around z8_GND_5296; the GOODS and CANDELS *HST* images are $3''$ on a side, while the S-CANDELS *Spitzer*/IRAC 3.6 and 4.5 μm images are $15''$ on a side. We also show mean stacks of the five optical bands and the three near-IR bands, the latter of which shows that this galaxy appears to have a clumpy morphology. This galaxy is not detected in any optical band, even when stacked together, which is strongly suggestive of a redshift greater than 7. The IRAC bands show a faint detection in the 3.6 μm band, and a strong detection in the 4.5 μm band. This signature is expected if strong [O III] emission is present in the 4.5 μm band, which would be the case for a strongly star-forming galaxy at $z \sim 7.5$, with sub-Solar (though still significant) metal content (0.2–0.4 Z$_\odot$). The bottom plot shows the results of our photometric redshift analysis placing z8_GND_5296 at $7.3 < z < 8.1$ at 95% confidence, which encompasses our measured spectroscopic redshift (denoted by the vertical line). We show both the probability distribution function as well as the values of χ^2 at each redshift; though a low-redshift solution is possible, it is strongly disfavored, with the high-redshift solution being $\sim 7 \times 10^9$ more probable.
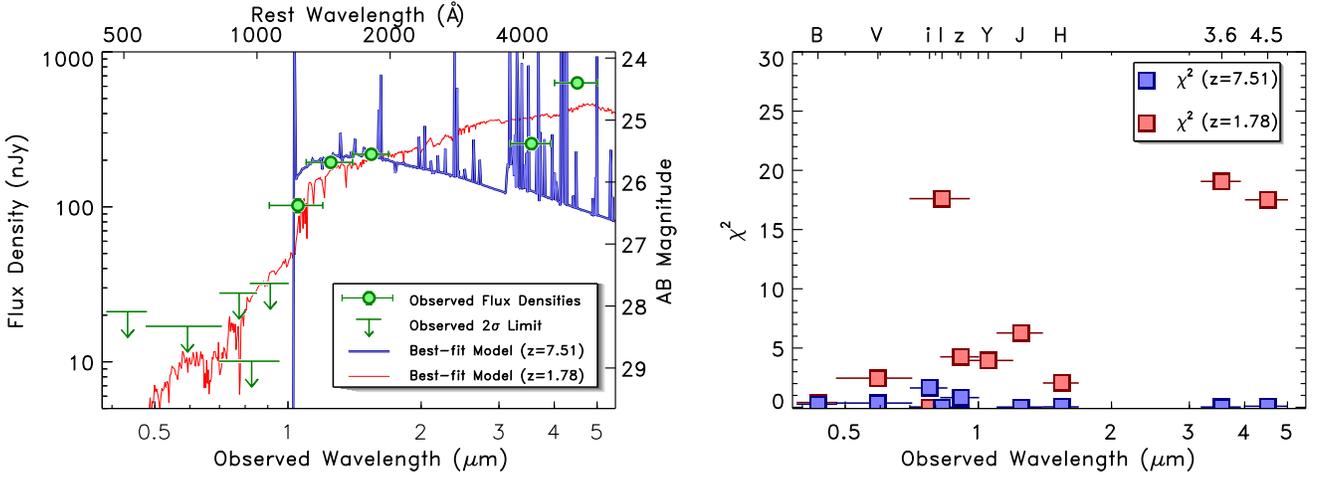
Figure 3 | Spectral Energy Distribution Fitting of z8_GND_5296. Left) The results of fitting stellar population models to the observed photometry of z8_GND_5296. The best-fit model for $z = 7.51$ (if our observed line is Lyα) is shown as the blue spectrum, while the alternate redshift of $z = 1.78$ (if the line is [O II]) is shown by the red spectrum. The horizontal error bars denote the bandpass FWHMs. Right) The measured χ^2 for each band for the best-fit model at each redshift. The lack of detectable optical flux, particularly in the deep F814W image, as well as the extremely red IRAC color, strongly favor the high-redshift solution (reduced $\chi^2[z = 7.51] = 0.8$ versus $\chi^2[z = 1.78] = 14.7$). Additionally, the low-redshift model exhibits no star-formation, thus this stellar population should not have detectable [O II] emission. The best-fitting high-redshift model shows that this galaxy has a stellar mass of about 10^9 M$_\odot$, with a 10-Myr-averaged star-formation rate (SFR) of ~330 M$_\odot$ yr^{-1} (68% C.L. 320 − 1040 M$_\odot$ yr^{-1}). The large SFR may be responsible for the ability of Lyα to escape this galaxy.

3.6μm band, but it is predicted to be about 5× fainter than [O III], and thus does not affect the 3.6μm band as much as [O III] affects 4.5μm.

This galaxy is forming stars at a very high rate, with a "mass-doubling" time of at most 4 Myr. The most recent estimates [17] at $z \approx 7$ find that galaxies with stellar masses of 5×10^9 M$_\odot$ typically have specific SFRs (sSFR = SFR divided by stellar mass) ~10^{-8} yr^{-1}. This galaxy is a factor of five less massive, yet its sSFR is a factor of 30 greater, at 3×10^{-7} yr^{-1}, implying that z8_GND_5296 is undergoing a significant starburst. Additionally, estimates of the SFR functions[9] show that a typical galaxy at $z \sim 7$ has a SFR = 10 M$_\odot$ yr^{-1}; the measured SFR of z8_GND_5296 is a factor of >30× greater. If this SFR function is accurate, the expected space density per co-moving Mpc^3 for this galaxy would be $\ll 10^{-5}$. The implied rarity of this galaxy could imply that it is the progenitor of some of the most massive systems in the high-redshift universe. However, the $z = 7.213$ galaxy GN-108036[3], also in GOODS-North, also has an implied SFR > 100 M$_\odot$ yr^{-1}. While the current statistics are poor, the presence of these two galaxies in a relatively small survey field suggests that the abundance of galaxies with such large star formation rates may have been underestimated. ' z8_GND_5296 and GN-108036 also both have young inferred ages and IRAC colors indicative of strong [O III] emission. Given the difficulty of detecting Lyα emission at $z \geq 6.5$, it is interesting that these highest redshift Lyα-detected galaxies appear to have extreme SFRs and high [O III] emission. It may be that a high SFR and/or a high excitation are necessary conditions for Lyα escape in the distant universe, perhaps through blowing holes in the ISM, allowing both Lyα and ionizing photons to escape. An outflow in the ISM of 200-300 km s^{-1} could clear a hole in this galaxy in about 3–5 Myr, or perhaps even sooner if the galaxy is undergoing a merger, which could preferentially clear some lines of sight for Lyα to escape.

Finally, we examine the lack of detected Lyα lines in our full dataset. If the Lyα EW distribution continues its observed increase [18] from $3 < z < 6$ out to $z \sim 7$–8, we should have detected Lyα emission from 6 galaxies. Our single detection rules out this EW distribution at 2.5σ significance. This confirms previous results at $z \sim 6.5$. [3,5,6,8] This perceived lack of Lyα emission was previously inferred to be due to a rapidly increasing neutral fraction in the IGM at $z > 6.5$, as contamination by lower redshift interlopers is likely not dominant at $z = 7$ given the low contamination rate at $z = 6$. [8] However, most other observations are consistent with an IGM neutral fraction $\leq 10\%$ [19,20] at

Table 1: Lyα Spectroscopically Confirmed Galaxies at $z > 7$

$z_{Ly\alpha}$	M_{UV}	Rest EW$_{Ly\alpha}$ (Å)	Reference
7.508	−21.2	8	This Work
7.215	−22.4	15	Shibuya et al. 2012
7.213	−21.8	33	Ono et al. 2012
7.109	−20.4†	50	Vanzella et al. 2010
7.045	−21.1†	65	Schenker et al. 2012
7.008	−20.6†	64	Vanzella et al. 2010

Table 1 | †We compute UV absolute magnitudes for the Vanzella et al. and Schenker et al. galaxies using the Lyα-corrected Y-band magnitudes and J-band magnitude, respectively.

$z = 7$.

An alternative explanation for at least park of the Lyα deficit may be gas within the galaxies. A high gas-to-stellar mass ratio may be consistent with the very high SFR of z8_GND_5296, as galaxies should not have SFRs (for long periods) exceeding their average gas accretion rate from the IGM (which is set by the total baryonic mass). For the inferred stellar mass and redshift, z8_GND_5296 must have a gas reservoir of ~50× the stellar mass to give an accretion rate comparable to the SFR.[21] If true, this galaxy would have gas surface densities similar to the most gas-rich galaxies in the local universe, and its SFR would be consistent with local relations between the gas and SFR surface densities[22]. The large gas-to-stellar mass ratio could be due to low metallicities at earlier times which may initially inhibit star-formation allowing the formation of such a large gas reservoir.[23] If such high gas-to-stellar mass ratios are common amongst $z > 7$ galaxies, it could explain the relative paucity of Lyα emission in our observations. Clearly direct observations of the gas properties of distant galaxies are required to make progress understanding both the fueling of star formation, and the escape of Lyα photons.

1. Vanzella, E. *et al.* Spectroscopic Confirmation of Two Lyman Break Galaxies at Redshift Beyond 7. *ApJL* **730**, L35 (2011).

2. Schenker, M. A. *et al.* Keck Spectroscopy of Faint $3 < z < 8$ Lyman Break Galaxies: Evidence for a Declining Fraction of Emission Line Sources in the Redshift Range $6 < z < 8$. *ApJ* **744**, 179 (2012).

3. Ono, Y. *et al.* Spectroscopic Confirmation of Three z-dropout Galaxies at z = 6.844-7.213: Demographics of Lyα Emission in z ∼ 7 Galaxies. *ApJ* **744**, 83 (2012).

4. Shibuya, T. *et al.* The First Systematic Survey for Lyα Emitters at z = 7.3 with Red-sensitive Subaru/Suprime-Cam. *ApJ* **752**, 114 (2012).

5. Kashikawa, N. *et al.* The End of the Reionization Epoch Probed by Lyα Emitters at z = 6.5 in the Subaru Deep Field. *ApJ* **648**, 7–22 (2006).

6. Iye, M. *et al.* A galaxy at a redshift z = 6.96. *Nature* **443**, 186–188 (2006).

7. Ouchi, M. *et al.* Statistics of 207 Lyα Emitters at a Redshift Near 7: Constraints on Reionization and Galaxy Formation Models. *ApJ* **723**, 869–894 (2010).

8. Pentericci, L. *et al.* Spectroscopic Confirmation of z ∼ 7 Lyman Break Galaxies: Probing the Earliest Galaxies and the Epoch of Reionization. *ApJ* **743**, 132 (2011).

9. Smit, R. *et al.* The Star Formation Rate Function for Redshift z ˜ 4-7 Galaxies: Evidence for a Uniform Buildup of Star-forming Galaxies during the First 3 Gyr of Cosmic Time. *ApJ* **756**, 14 (2012).

10. Grogin, N. A. *et al.* CANDELS: The Cosmic Assembly Near-infrared Deep Extragalactic Legacy Survey. *ApJS* **197**, 35 (2011).

11. Koekemoer, A. M. *et al.* CANDELS: The Cosmic Assembly Near-infrared Deep Extragalactic Legacy Survey – The Hubble Space Telescope Observations, Imaging Data Products, and Mosaics. *ApJS* **197**, 36 (2011).

12. McLean, I. S. *et al.* MOSFIRE, the multi-object spectrometer for infra-red exploration at the Keck Observatory. In *SPIE Conference Series*, vol. 8446 of *SPIE Conference Series* (2012).

13. Finkelstein, S. L. *et al.* On the Stellar Populations and Evolution of Star-forming Galaxies at 6.3 ≤ z ≤ 8.6. *ApJ* **719**, 1250–1273 (2010).

14. McLure, R. J. *et al.* Galaxies at z = 6-9 from the WFC3/IR imaging of the Hubble Ultra Deep Field. *MNRAS* **403**, 960–983 (2010).

15. Finkelstein, S. L. *et al.* CANDELS: The Evolution of Galaxy Rest-frame Ultraviolet Colors from z = 8 to 4. *ApJ* **756**, 164 (2012).

16. McLure, R. J. *et al.* A new multifield determination of the galaxy luminosity function at z = 7-9 incorporating the 2012 Hubble Ultra-Deep Field imaging. *MNRAS* **432**, 2696–2716 (2013).

17. Stark, D. P. *et al.* Keck Spectroscopy of 3 < z < 7 Faint Lyman Break Galaxies: The Importance of Nebular Emission in Understanding the Specific Star Formation Rate and Stellar Mass Density. *ApJ* **763**, 129 (2013).

18. Stark, D. P., Ellis, R. S. & Ouchi, M. Keck Spectroscopy of Faint 3>z>7 Lyman Break Galaxies: A High Fraction of Line Emitters at Redshift Six. *ApJL* **728**, L2 (2011).

19. Bolton, J. S. *et al.* How neutral is the intergalactic medium surrounding the redshift z = 7.085 quasar ULAS J1120+0641? *MNRAS* **416**, L70–L74 (2011).

20. Finkelstein, S. L. *et al.* CANDELS: The Contribution of the Observed Galaxy Population to Cosmic Reionization. *ApJ* **758**, 93 (2012).

21. Dekel, A. *et al.* Toy Models for Galaxy Formation versus Simulations. *ArXiv e-prints* (2013).

22. Kennicutt, R. C. & Evans, N. J. Star Formation in the Milky Way and Nearby Galaxies. *ARAA* **50**, 531–608 (2012).

23. Krumholz, M. R. & Dekel, A. Metallicity-dependent Quenching of Star Formation at High Redshift in Small Galaxies. *ApJ* **753**, 16 (2012).

24. Giavalisco, M. *et al.* The Rest-Frame Ultraviolet Luminosity Density of Star-forming Galaxies at Redshifts z>3.5. *ApJL* **600**, L103–L106 (2004).

25. Oke, J. B. & Gunn, J. E. Secondary standard stars for absolute spectrophotometry. *ApJ* **266**, 713–717 (1983).

26. Bertin, E. & Arnouts, S. SExtractor: Software for source extraction. *A&AS* **117**, 393–404 (1996).

27. Guo, Y. *et al.* CANDELS Multi-Wavelength Catalogs: Source Detection and Photometry in the GOODS-South Field. *ApJ Submitted* (2013).

28. Brammer, G. B., van Dokkum, P. G. & Coppi, P. EAZY: A Fast, Public Photometric Redshift Code. *ApJ* **686**, 1503–1513 (2008).

29. Tanvir, N. R. *et al.* A γ-ray burst at a redshift of z˜8.2. *Nature* **461**, 1254–1257 (2009).

30. Salvaterra, R. *et al.* GRB090423 at a redshift of z˜8.1. *Nature* **461**, 1258–1260 (2009).

31. Lehnert, M. D. *et al.* Spectroscopic confirmation of a galaxy at redshift z = 8.6. *Nature* **467**, 940–942 (2010).

32. Bunker, A. J. *et al.* VLT/XSHOOTER and Subaru/MOIRCS spectroscopy of HUDF.YD3: no evidence for Lyman α emission at z = 8.55. *MNRAS* **430**, 3314–3319 (2013).

33. Shapley, A. E., Steidel, C. C., Pettini, M. & Adelberger, K. L. Rest-Frame Ultraviolet Spectra of z∼3 Lyman Break Galaxies. *ApJ* **588**, 65–89 (2003).

34. Steidel, C. C. *et al.* The Structure and Kinematics of the Circumgalactic Medium from Far-ultraviolet Spectra of z ∼= 2-3 Galaxies. *ApJ* **717**, 289–322 (2010).

35. Kurucz, R. L. *SYNTHE spectrum synthesis programs and line data* (1993).

36. Storey, P. J. & Zeippen, C. J. Theoretical values for the [Oiii] 5007/4959 line-intensity ratio and homologous cases. *MNRAS* **312**, 813–816 (2000).

37. Osterbrock, D. E. *Astrophysics of Gaseous Nebulae and Active Galactic Nuclei* (Mill Valley: University Science Books, 1989).

38. Rhoads, J. E., Hibon, P., Malhotra, S., Cooper, M. & Weiner, B. A Lyα Galaxy at Redshift z = 6.944 in the COSMOS Field. *ApJL* **752**, L28 (2012).

39. McLinden, E. M. *et al.* First Spectroscopic Measurements of [O III] Emission from Lyα Selected Field Galaxies at z ˜ 3.1. *ApJ* **730**, 136 (2011).

40. Finkelstein, S. L. *et al.* The HETDEX Pilot Survey. III. The Low Metallicities of High-redshift Lyα Galaxies. *ApJ* **729**, 140 (2011).

41. Hashimoto, T. *et al.* Gas Motion Study of Lyα Emitters at z ˜ 2 Using FUV and Optical Spectral Lines. *ApJ* **765**, 70 (2013).

42. Dijkstra, M., Mesinger, A. & Wyithe, J. S. B. The detectability of Lyα emission from galaxies during the epoch of reionization. *MNRAS* **414**, 2139–2147 (2011).

43. Rhoads, J. E. *et al.* First Results from the Large-Area Lyman Alpha Survey. *ApJL* **545**, L85–L88 (2000).

44. Gawiser, E. *et al.* The Physical Nature of Lyα-emitting Galaxies at z=3.1. *ApJL* **642**, L13–L16 (2006).

45. Koopmans, L. V. E., Treu, T., Bolton, A. S., Burles, S. & Moustakas, L. A. The Sloan Lens ACS Survey. III. The Structure and Formation of Early-Type Galaxies and Their Evolution since z ˜ 1. *ApJ* **649**, 599–615 (2006).

46. Ashby, M. L. N. *et al.* SEDS: The Spitzer Extended Deep Survey. Survey Design, Photometry, and Deep IRAC Source Counts. *ApJ* **769**, 80 (2013).

47. Peng, C. Y., Ho, L. C., Impey, C. D. & Rix, H.-W. Detailed Decomposition of Galaxy Images. II. Beyond Axisymmetric Models. *AJ* **139**, 2097–2129 (2010).

48. Finkelstein, K. D. *et al.* Probing the Star Formation History and Initial Mass Function of the z ∼ 2.5 Lensed Galaxy SMM J163554.2+661225 with Herschel. *ApJ* **742**, 108 (2011).

49. Bruzual, G. & Charlot, S. Stellar population synthesis at the resolution of 2003. *MNRAS* **344**, 1000–1028 (2003).

50. Reddy, N. *et al.* GOODS-Herschel Measurements of the Dust Attenuation of Typical Star-forming Galaxies at High Redshift: Observations of Ultraviolet-selected Galaxies at z ∼ 2. *ApJ* **744**, 154 (2012).

51. Tilvi, V. *et al.* Discovery of Lyman Break Galaxies at z ˜ 7 from the zFourGE Survey. *ApJ* **768**, 56 (2013).

52. Oesch, P. A. *et al.* A Rest-frame Optical View on z˜4 Galaxies I: Color and Age Distributions from Deep IRAC Photometry of the IUDF10 and GOODS Surveys. *ArXiv e-prints* (2012).

53. Calzetti, D. *et al.* The Dust Content and Opacity of Actively Star-forming Galaxies. *ApJ* **533**, 682–695 (2000).

54. Pei, Y. C. Interstellar dust from the Milky Way to the Magellanic Clouds. *ApJ* **395**, 130–139 (1992).

55. Papovich, C., Finkelstein, S. L., Ferguson, H. C., Lotz, J. M. & Giavalisco, M. The rising star formation histories of distant galaxies and implications for gas accretion with time. *MNRAS* **412**, 1123–1136 (2011).

56. Finlator, K., Oppenheimer, B. D. & Davé, R. Smoothly rising star formation histories during the reionization epoch. *MNRAS* **410**, 1703–1724 (2011).

57. Jaacks, J., Choi, J.-H., Nagamine, K., Thompson, R. & Varghese, S. Steep faint-end slopes of galaxy mass and luminosity functions at z¿ 6 and the implications for reionization. *MNRAS* **420**, 1606–1620 (2012).

58. Inoue, A. K. Rest-frame ultraviolet-to-optical spectral characteristics of extremely metal-poor and metal-free galaxies. *MNRAS* **415**, 2920–2931 (2011).

59. Kennicutt, R. C., Jr. Star Formation in Galaxies Along the Hubble Sequence. *ARAA* **36**, 189–232 (1998).

60. Bouwens, R. J. *et al.* UV-continuum Slopes at z ∼ 4-7 from the HUDF09+ERS+CANDELS Observations: Discovery of a Well-defined UV Color-Magnitude Relationship for z >= 4 Star-forming Galaxies. *ApJ* **754**, 83 (2012).

61. Neistein, E. & Dekel, A. Merger rates of dark matter haloes. *MNRAS* **388**, 1792–1802 (2008).

62. Dekel, A., Sari, R. & Ceverino, D. Formation of Massive Galaxies at High Redshift: Cold Streams, Clumpy Disks, and Compact Spheroids. *ApJ* **703**, 785–801 (2009).

63. Alexander, D. M. *et al.* The Chandra Deep Field North Survey. XIII. 2 Ms Point-Source Catalogs. *AJ* **126**, 539–574 (2003).

64. Finkelstein, S. L., Rhoads, J. E., Malhotra, S. & Grogin, N. Lyman Alpha Galaxies: Primitive, Dusty, or Evolved? *ApJ* **691**, 465–481 (2009).

65. Laursen, P., Sommer-Larsen, J. & Razoumov, A. O. Intergalactic Transmission and Its Impact on the Lyα Line. *ApJ* **728**, 52 (2011).

Author Contributions   S.L.F. wrote the text, obtained and reduced the data, and led the initial observing proposal. C.P. and M.D. assisted with the analysis of the data. M.S. and V.T. assisted with the observation planning and implementation. K.D.F. performed the *Spitzer*/IRAC photometry. A.M.K. was responsible for the reduction of the optical and near-IR imaging data used to select the sample. G.G.F., M.L.N.A. and S.P.W. obtained and reduced the mid-infrared data. B.J.W. provided grism spectroscopic information. B.M., H.C.F., M.G, N.R., A.D., A.F., N.A.G., J.-S. H., D.K., and M.R. have contributed in their roles as members of the CANDELS and S-CANDELS teams, and assisted with the planning and interpretation of the observations.

SUPPLEMENTARY INFORMATION

1 Sample Selection

Our sample of high-redshift galaxies in the GOODS-North field was selected using an updated version of the criteria presented in previous papers;[15,20] the full sample will be published in Finkelstein et al. (2013, in prep). These papers can be consulted for more details, but here we briefly recap our process.

The optical imaging comes from the GOODS survey,[24] and we used the v2.0 ACS imaging, consisting of mosaics in the F435W, F606W, F775W and F850LP filters. The near-infrared data comes from the CANDELS survey, and we used the CANDELS team early data products (v0.1) in the F105W, F125W and F160W filters. The CANDELS survey is obtaining data at two depths, denoted as "WIDE" and "DEEP". The imaging used here consists of the full depth in the Northwest WIDE region, and about half of the full depth of the DEEP region. The 5σ limiting magnitudes, measured in $0.4''$-diameter apertures, for the ACS bands are: 28.1, 28.3, 27.8 and 27.7, respectively (all magnitudes are quoted in the AB system[25]). For the three WFC3 bands, the existing DEEP 5σ depths are 27.9, 27.9 and 27.7, while for the WIDE region, the depths are 27.4, 27.4 and 27.3, respectively. Additionally, we add to our analysis new, extremely deep, optical data obtained with ACS in parallel to the CANDELS observations. These data were obtained in the F814W filter, and have an exposure time of 57,000 s at the position of our source, showing no detectable flux with a $0.4''$-diameter aperture 5σ depth of 28.8. We created photometry catalogs with the Source Extractor software,[26] using a weighted sum of the F125W and F160W images as the detection image. We measured colors in small elliptical apertures, setting the Kron aperture parameters to Kron_fact=1.2 and min_radius=1.7. Aperture corrections were measured in the F160W band by comparing the flux in this small aperture to that in the default MAG_AUTO aperture, which is representative of the total flux. Photometry was performed on the DEEP and WIDE regions separately. Photometry errors were obtained by providing Source Extractor with accurate RMS images.

No RMS map was available for the F814W data, but we followed the same procedures used to calibrate noise maps for the standard CANDELS HST data products[27]. We measured the RMS and auto-correlation function of the background noise near the position of our object, after masking out sources. We scaled the correlation-corrected RMS to the number of pixels in the elliptical photometry aperture, finding a total 1σ F814W flux uncertainty of 5 nJy. This is a factor of about $3\times$ deeper than the GOODS F775W or F850LP imaging at this position. These F814W data were not available at the time of our observations, so here we add the F814W non-detection to the photometric redshift and spectral energy distribution analysis for z8_GND_5296, assuming a flux error of 5 nJy.

To select our galaxy sample, we utilized a photometric redshift fitting technique, using the EAZY software package[28] to estimate the likely redshift (and associated redshift probability distribution function, $\mathcal{P}[z]$) by finding the best-fitting combination of redshifted galaxy spectral templates. Both our DEEP and WIDE catalogs were run through EAZY. We then selected samples with $\Delta z \sim 1$ centered at $z_{sample} = 6, 7$ and 8. Rather than using the best-fit photometric redshift to select our galaxy sample, we utilized the full redshift probability distribution function. For a given object to be in our sample, it had to meet all of the following criteria:

- Signal-to-noise in both the F125W and F160W bands ≥ 3.5.

- $\geq 70\%$ of the integral of $\mathcal{P}(z)$ in the primary redshift solution.

- $\int \mathcal{P}(z_{sample} \pm 0.5)dz \geq 0.25$

- $\int \mathcal{P}(z_{sample} \pm 0.5)dz \geq \int \mathcal{P}(z_{sample\pm 1} \pm 0.5)$ dz

- $\int \mathcal{P}(z > z_{sample} - 2)dz \geq 0.5$

- $z_{best} > z_{sample} - 2$

- $\chi^2 < 60$

These are very similar to the criteria used in our previous publications, and they have been shown to produce samples which match up very well with available spectroscopic redshifts.[15]

The selected sources were visually inspected to reject artifacts such as diffraction spikes and oversplit regions of bright galaxies. Additionally, the colors of galaxy candidates were compared to the expected colors of M, L and T-dwarf stars, and any sources with star-like colors which were also unresolved were rejected from the sample. Finally, the optical bands were also inspected to ensure that they visually appeared to contain no significant ($>1.5\sigma$) flux (in practice, sources with significant optical flux would have already been rejected by our selection criteria). Our final galaxy samples consist of 175 candidate galaxies at $z \approx 6$, 85 at $z \approx 7$ and 25 at $z \approx 8$.

2 Spectroscopic Followup Sample

From our parent sample of candidate galaxies, we selected those for spectroscopic followup with MOSFIRE via two criteria: 1) apparent F160W magnitude, and 2) maximizing $\int \mathcal{P}(7.0 < z < 8.2)dz$ (which corresponds to the redshift range placing Lyα in the MOSFIRE Y-band grating). We first prioritized based on brightness, and then within each magnitude bin, we prioritized based on the highest value of the integral defined above. We input these catalogs into the MAGMA software[F1], which was created by the MOSFIRE team to design mask configurations. The software searches a large (user-defined) parameter space in both right ascension, declination and position angle to maximize the total priority of sources. We designed two masks: GOODSN_Mask1, with a position angle of 34 degrees, containing 24 candidate high-redshift galaxies, and GOODSN_Mask2, with a position angle of -9.5 degrees, containing 19.

3 Observations and Data Reduction

Our observations took place on UT 18-19 April 2013 under clear, mostly photometric conditions. We used MOSFIRE with the Y-band grating, which observes $\sim 0.97 - 1.12\ \mu$m, and set the slit widths to $0.7''$. We observed each configuration for one night, taking 180 sec exposures with an ABAB dither pattern, with dither positions separated by $2.5''$, yielding a total exposure time of 5.6 hr for the first configuration and 4.45 hr for the second. The data were reduced using the MOSFIRE data reduction pipeline[F2], which in brief calculates a wavelength solution using the night sky lines, performs sky subtraction, flat-fielding and rectification, and saves each two-dimensional slit spectrum as a single image. We examined the expected slit position for each object by eye to search for detected emission lines. Given our dither pattern, true features are identifiable with a positive signal and two negative signals on each side in the spatial dimension, due to the sky subtraction (i.e., each negative signal contains half of the amplitude of the positive signal). We identified four plausible emission lines from the first mask, and three from the second mask.

3.1 One-Dimensional Spectral Extraction For these seven sources, we performed one-dimensional spectral extraction with a $1.6''$ box in the spatial dimension ($\sim 2\times$ the seeing during the run, which varied from 0.6 - $0.8''$). The error spectrum was similarly extracted from the inverse variance spectrum created by the pipeline. To ensure that the error spectrum accurately matched the errors in the object spectrum, we scaled the error spectrum to be representative of noise variations in

---

[F1] http://www2.keck.hawaii.edu/inst/mosfire/magma.html
[F2] http://code.google.com/p/mosfire/

the object spectrum, by measuring the standard deviation in the signal-to-noise of pixels in regions clear of sky emission lines, and scaled the error spectrum so that this equaled unity. To determine the significance of the seven extracted lines, we fit a Gaussian function using the MP-FIT IDL package[F3], finding that only one object had a line detected at $> 5\sigma$ significance. This object, called z8_GND_5296 in our catalog, is measured to have an emission line at $\lambda = 1.0343$ μm with a significance of 7.8σ (Figure 1). Assuming this line is Lyα places this object at $z = 7.5078 \pm 0.0004$, making this current the highest redshift galaxy that has been spectroscopically confirmed via Lyα. There has been a published spectroscopic confirmation of the gamma ray burst (GRB) 090423 at $z = 8.2$, confirmed via continuum spectroscopy of the Lyman break,[29,30], though due to its very nature this object cannot be re-observed. Additionally, though a spectroscopic redshift of $z = 8.56$ for a galaxy has been claimed,[31] subsequent observations have shown this to be spurious.[32] The properties of z8_GND_5296 are summarized in Table S1. We note that the uncertainty on the redshift denotes the uncertainty on centroiding the line. However, as shown at lower redshift, Lyα is frequently detected at 200–800 km s^{-1} redward of the systemic redshift[33,34], thus the systemic redshift for this system may be a few hundred km s^{-1} lower.

The MOSFIRE data reduction pipeline provides a nominal guess for the central row for each objects spectrum, accounting for differing vertical positions in the slit. To ensure that our extracted emission line in the spectrum of z8_GND_5296 is in the correct spatial position, we used three sources in our mask with well-detected continuum; one was a star, while the other two were $z \sim 1$ galaxies placed in the mask as fillers. We found that all three sources had centroids $\sim$4–5 pixels below the pipeline guess, with a mean offset of 4.7 pixels. Examining the emission line in the 2D spectrum of z8_GND_5296, we find that the line also has a centroid offset by the pipeline guess by 4.7 pixels. Thus, we conclude that the observed emission line is at the expected position for the high-redshift galaxy we intended to observe, and we use this offset position as the extraction center. As shown in Figure 2, there are no other sources in the slit, though there are two galaxies located $2.3''$ and $3.2''$ southwest of our target. The closer galaxy would lie $1.1''$ off the slit center, and would be offset by $1.9''$ along the slit from our object, which corresponds to $\sim$10 pixels in the 2D spectrum. Any emission from these objects which happened to fall in the slit would thus be clearly separated from our observed emission line. In Section S4.3, we find that both of these nearby galaxies have spectroscopic redshifts of 0.39, which would not place any known emission line near 1.0343 μm.

In order to examine the possibility of a false positive detection, we examined the signal-to-noise spectrum, smoothed by the velocity width of our spectrum, and scaled the such that the value at the peak of our detected line is equal to the integrated signal-to-noise of the line of 7.8, as illustrated in Figure S1. We searched the entire spectrum for apparently significant negative features; these would be due to noise, and the lack of such features provides greater confidence that our observation represents a true emission line from the object z8_GND_5296, while the lack of positive features other than our identified Lyα line provides further confidence that the line is in fact Lyα.

3.2 Flux Calibration We flux calibrated the spectrum of z8_GND_5296 using observations of the standard star HIP 56157, with a spectral type of A0V, which we observed in a single long slit directly before our science observations during our first night of observing. We obtained four spectra of this star with an ABAB dither pattern, with each exposure consistent of 10 2s co-additions, to guard against persistence and non-linearity. These observations were reduced in the same manner as our masks described above, and extracted into a one-dimensional spectrum with the same size extraction box as that

[F3]http://www.physics.wisc.edu/~craigm/idl/fitting.html
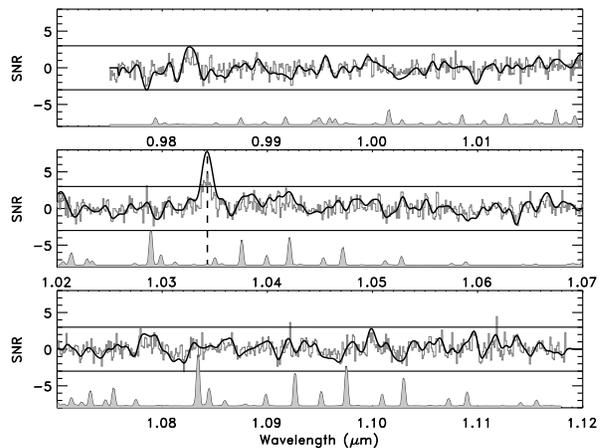
Figure S1 | Emission line signal-to-noise test. The results of a signal-to-noise test for the one-dimensional spectrum of z8_GND_5296 (each row represents a different region of the spectrum). We divided the object spectrum by the error spectrum, smoothed by the velocity width of our observed line, and normalized the result so that the value at the peak of the Lyα line equaled the measured integrated line signal-to-noise of 7.8. The horizontal lines denote the $\pm 3\sigma$ points, and the gray filled spectrum denotes the (arbitrarily scaled) sky emission. Only the detected emission line has a |signal-to-noise| >3; the absence of negative fluctuations at this level, which would be due to noise, gives confidence in the real nature of this emission line.

used on our primary observations.

We derived the flux calibration array by taking a A0V Kurucz[35] model spectrum, and scaling it to match the integrated 2MASS magnitude for this star, interpolating among the J, H, and K 2MASS magnitudes to obtain the magnitude appropriate for our spectral range at 1.05 μm ($m_{1.05\mu m, AB} = 8.08$). We then created a calibration array by dividing this scaled model spectrum by our observed spectrum, interpolating over intrinsic stellar absorption features common to both spectra. The final array was then multiplied by our object spectrum (both normalized by their respective exposure times), which both flux calibrated our object spectrum, and corrected for telluric absorption features. Nominally, this procedure also corrects for slit losses, but only in the case when the seeing during both the standard and object observations was the same. In our case, the seeing was moderately different; the median seeing during the mask observations was $0.65''$, while it was $0.85''$ during the standard observations. Thus an additional aperture correction of 1.22 was applied to account for the seeing differences.

We measured the line flux of our detected emission line by again fitting a Gaussian with MPFIT, only now to the calibrated spectrum. We measured a line flux of 2.64×10^{-18} erg s^{-1} cm^{-2}. We had expected to achieve a 5σ limiting line flux of 2.1×10^{-18} erg s^{-1} cm^{-2} in 5.5 hr (scaled from our initial expectation of 2.0×10^{-18} erg s^{-1} cm^{-2} in 6 hr). Given our measured line flux, and signal-to-noise reported above of 7.8, this would imply a 5σ limiting line flux of 1.7×10^{-18} erg s^{-1} cm^{-2}. While this may be the case, there is an additional systematic uncertainty in our flux calibration, as the counts varied by $\sim$15% in the four individual observations of the standard star. Taking this into account, our measured line flux is 2.64 ± 0.34 (photometric) ± 0.40 (systematic) $\times 10^{-18}$ erg s^{-1} cm^{-2}. Accounting for the systematic uncertainty, our measured line flux is consistent with that expected for a signal-to-noise=7.8 detection at $\sim 1.2\sigma$. The flux calibration does not have an impact on our primary science results, but we will use this calibrated line flux below when discussing the Lyα equivalent width.

4 Line Identification

Although our photometric redshift favors Lyα as the identification for our detected emission line in the spectrum of z8_GND_5296, here

Table S1: Summary of Spectroscopically Confirmed Galaxy

Object	R.A. (J2000)	Dec (J2000)	mag$_{F160W}$ (AB)	Photo-z 68% C.L.	λ_{line} (Å)	$z_{Ly\alpha}$	SNR$_{line}$
z8_GND_5296	12:36:37.90	62:18:08.5	25.6	7.5 – 7.9	10342.6	7.508	7.8

we examine the alternatives. Other plausible alternatives to Lyα (i.e., lines that have been observed to be reasonably strong at high-redshift) are [O II] $\lambda\lambda$ 3726,3729, Hβ λ4861, [O III] λ4959, [O III] λ5007, and Hα λ6563 (other lines are possible if the object is an AGN, but this is not likely due to the lack of X-ray or long-wavelength detections; see below). Of these alternatives, Hβ and [O III] can be ruled out, as were our detected line one of these three, the other lines should be observed as well. Specifically, were our observed line [O III] λ5007, we would expect to see [O III] λ4959 at 10243.5 Å, which is a region clear of sky emission. We simulated a [O III] λ4959 line at this position in our spectrum, with a line strength 2.98$\times$ less than that of the λ5007 line,[36] and found that such a line would have been detected at 4.1σ, thus we rule out [O III] λ5007 as the identification of our detected line. Additionally, we can rule out both [O III] lines, as well as Hα, as they are not located near strong continuum breaks. As seen in Figure 3, we have detected a large photometric break at $\lambda \sim 1\mu m$. We interpret it as the Lyman break, but it could also be the Balmer break at 3646 Å due to a combination of the high-order Balmer series transitions, or the 4000 Å break due to metal absorption lines common in older stellar populations. Were this the case, then the detected line would be [O II].

As [OII] is a doublet, we examine the spectrum for signs of the second line. The ratio of the λ3726/λ3729 line strength varies from $\sim$0.5–1.5 in H II regions, with a typical ratio of order unity.[37] If our detected line was the red side of the doublet (at 3729 Å rest), we should detect the bluer line at 10334 Å (which is a clean region) at $>$10σ, and no line is seen. If the detected line is the bluer side of the doublet, then we would expect to see the redder line at 10351 Å. This would be directly under the sky line just to the red of our detected line, which hampers our ability to discern its presence. However, given the width of our detected line, if there were a second line under the sky line, we would expect to see excess flux just to the red side of the sky residual (i.e., the true line would be broader than the sky residual), in between the two sky lines. As shown in Figure S2, for line ratios of unity or greater, the observed spectrum can rule out the presence of the redder [O II] line. If the λ3726/λ3729 ratio is high; close to 1.5, then it becomes harder to rule out the presence of this line. However, there is should still be excess flux over that observed on either side of the sky line residual – in particular, on the red side of the sky line, we would have expected to see emission line flux at the $\sim$2σ level. Given the lack of detectable flux in this region, we conclude that the line is unlikely to be [O II]. However, given the unknown strength of any potential 3729 Å line, in the following we examine further evidence to differentiate between Lyα and [O II].

4.1 Line Asymmetry Another feature which could confirm the Lyα nature of this line would be any measured asymmetry. Lyα at high redshift is frequently observed to be asymmetric,[1,3] though it has been observed to be symmetric as well.[38] It is assumed that the asymmetry is caused by absorption of the blue half of the line by neutral hydrogen in the IGM. However, a few lines of evidence imply that internal processes in the galaxy may dominate the observed line profile. First, Lyα lines at $z \sim$ 2–3 have been observed to be asymmetric, at an epoch where the IGM absorption is much less. Second, also at $z \sim$ 2–3, where the systemic redshift can be measured via rest-frame optical nebular lines, Lyα is seen to reside $\sim$200-400 km s^{-1} to the red of the systemic redshift.[34,39–41] This is likely a result of interstellar winds driven by intense star-formation, as Lyα photons will preferentially escape after they have gained some net redshift, and are thus no longer
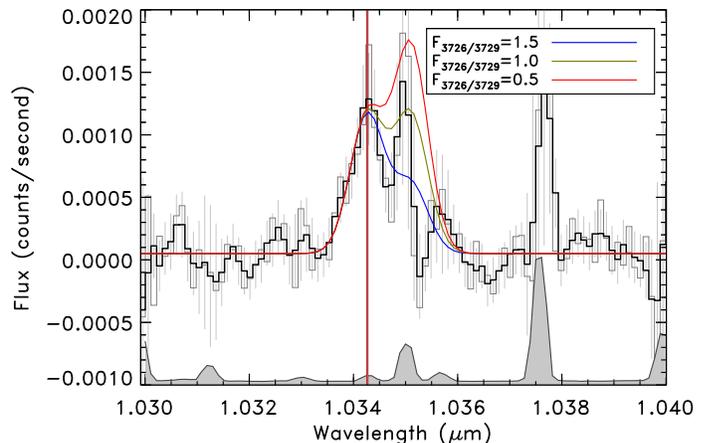
Figure S2 | [O II] Doublet. A zoomed in view of our source spectrum, overplotting hypothetical [O II] doublet lines for three values of the ratio between the line fluxes. Unless the [O II] 3729 Å line is substantially weaker than the 3726 Å line, we would have expected to see highly significant flux from the redder line. Even in the case where the redder line is 50% the strength of the bluer line, we should still have detected emission line flux redward of the sky line residual at the $\sim$2σ level.

resonantly scattered. This enables them to pass through neutral hydrogen both within the galaxy as well as in the IGM. Simulations have been run at $z > 8$ which have shown that with a wind velocity of $\sim$ a few hundred km s^{-1}, not only can Lyα emission be detectable from a mostly-neutral epoch, but it can be observed with a symmetric profile.[42] The large inferred SFR of our object is consistent with this scenario, as it is very likely driving a strong wind in the interstellar medium. Lyα is also symmetric in another bright ($m =$25.75) galaxy at z=6.944,[38] perhaps indicating that strong star-formation driven winds are common in these very luminous objects.

The asymmetry of our observed line is difficult to measure, given the night sky line residual to the red-side of our line. We measure the asymmetry of our emission line by fitting an asymmetric Gaussian function to the line profile, where the σ values on the blue and red side of line center are allowed to be different. We then quantify the asymmetry as the ratio of $\sigma_{red}/\sigma_{blue}$, measuring this ratio to be 1.2 $\pm$ 1.4, thus the measured asymmetry is of no significance. As a further test of our ability to measure any asymmetry in the detected emission line, we ran a series of simulations, placing mock emission lines with the same integrated line flux as our measured line, but with a known value of asymmetry, in our one-dimensional spectra. We investigated asymmetry values of both 2.0 and 1.5, and we placed these mock lines at three locations: 11082.6, 10119.4 and 10250.0 Å. The first two locations correspond to regions 7.4 Å blueward of a skyline with a similar amplitude to the skyline 7.4Å redward of our detected emission line; the first of these two has a positive sky-subtraction residual, while the second has a negative residual. The third wavelength is a region with no sky emission lines. In each of these six simulations, the measured asymmetry was consistent with unity (i.e., a symmetric line) at $\sim$1σ. The measured asymmetry values and associated uncertainties were 3.2 $\pm$ 2.8, 3.2 $\pm$ 2.1 and 3.9 $\pm$ 2.6 for the simulations where the input asymmetry value was 2.0, and 2.8 $\pm$ 4.7, 3.2 $\pm$ 2.0 and 2.3 $\pm$ 2.1 where the input asymmetry value was 1.5. Although each of these simulations
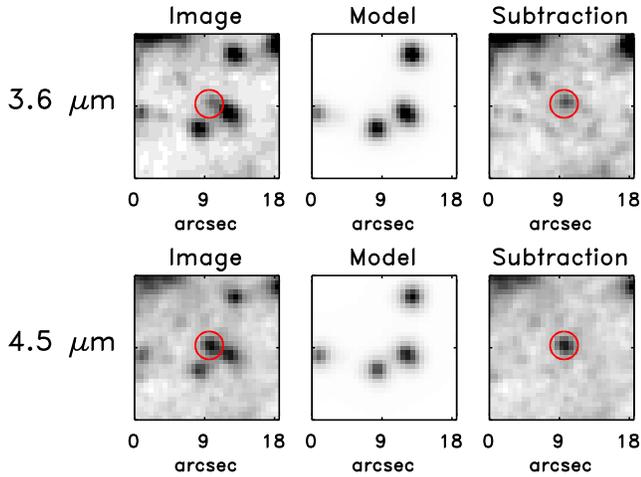
Figure S3 | IRAC photometry. 18.6″ stamps of z8_GND_5296 in the IRAC 3.6 (top row) and 4.5 (bottom row) μm bands, highlighting the de-blending algorithm we used to perform our source photometry. The first column is the image, the second is the GALFIT source model, and the third is the model-subtracted image, which clearly shows a significant detection for z8_GND_5296 in both bands, with minimal residuals from other sources. This fitting was straightforward, as the neighbors are relatively faint, and are well fit by point-sources. When we performed photometry, z8_GND_5296 was included in the model, thus the quoted magnitudes come from this point-source fitting method rather than a less accurate circular aperture.

results in a mean asymmetry value greater than unity, the very large uncertainties imply that our spectra are not of high enough signal-to-noise to detect a moderate amount of asymmetry were it present in the detected emission line. Deeper spectra with higher spectral resolution may make this possible, but given the presence of sky emission lines around our detected object, it may yet prove difficult. We thus conclude that we cannot rule out moderate asymmetry in our detected emission line.

4.2 Equivalent Width Photometric surveys for Lyα emitting galaxies at high redshift using narrowband filters frequently use the equivalent width of the line as a method to remove [O II] emitting "contaminants".[43,44] The dividing line used is commonly 20 Å in the rest frame of Lyα. As we do not detect the continuum in our spectrum, we must use the photometry to derive the continuum level near the detected emission line. We use the best-fitting model from our SED fitting (see the next subsection), to derive the continuum flux density just redward of Lyα (at a rest-frame wavelength of 1225 Å), which we find to be 4.15×10^{-20} erg s^{-1} cm^{-2} Å^{-1}. The EW is then defined as the ratio of the line flux to the continuum level, which we find to be 64 ± 8 (photometric) ± 10 (systematic) Å. If the line is Lyα at $z = 7.51$, this would correspond to a rest-frame EW = 7.5 Å, while for [O II] at $z = 1.78$, the rest-frame EW would be 23 Å. An emission line of this small EW would have a negligible impact on the integrated F105W magnitude, and it does not provide further evidence excluding the possibility of [O II], though it does support our primary conclusion that the equivalent width distribution at $z > 7$ has been drastically reduced.

4.3 Grism Spectroscopy and Lensing Most of the GOODS-North field, including the region of interest here, has been observed with *HST* WFC3 infrared slitless grism spectroscopy (Weiner et al. in preparation), covering the 1.1–1.65 μm spectral range. This range does not include the line at 1.0343 μm that we observe with MOSFIRE, but if that line were [OII] at $z = 1.78$ or [OIII] at $z = 1.07$, other emission lines (namely, [OIII]+Hβ or Hα+[NII], respectively) would fall within the grism spectral range. These are not observed, to an approximate 3σ flux limit of 3×10^{-17} erg s^{-1} cm^{-2}, neither in the spectrum of the faint galaxy z8_GND_5296, nor in the two galaxies that fall a few arcseconds

away to the southwest, near (but not on) the MOSFIRE slit (see Section S3). The closer (northeastern) of these two galaxies has a secure Keck DEIMOS spectroscopic redshift $z = 0.387$ (Stern et al. in preparation), which would not place any strong emission lines at 1.0343 μm. The second (southwestern) galaxy has no ground-based spectroscopy to our knowledge. Spectral templates cross-correlated with the WFC3 grism spectrum of this southwestern galaxy yield a possible redshift $z = 0.39 \pm 0.01$, largely due to a feature that would correspond to the [SIII] λ9069Å emission line at that redshift. While quite tentative, this is also consistent with the secure and accurate Keck redshift for the northeastern galaxy that is about 1 arcsec away, suggesting that the two may be a physical pair. In any case, there is no evidence to favor (and several reasons to discount) the possibility that the MOSFIRE emission line is due to contamination from a nearby foreground galaxy.

This nearby pair of galaxies is unlikely to act as a significant gravitational lens. At the spectroscopic redshift of $z = 0.39$ for both galaxies, we measure stellar masses from SED fitting for the NE galaxy of 5.8×10^7 M$_\odot$, and for the SW galaxy of 1.7×10^7 M$_\odot$. To determine whether these could plausibly magnify our $z = 7.51$ galaxy, we compute their Einstein radius, assuming a lens redshift of $z = 0.39$, and a source redshift of $z = 7.51$. For this calculation, we require the total mass of the galaxies, including dark matter, which we conservatively assume is $10\times$ the stellar mass (cf. compare to samples of massive galaxies in strong lensing surveys that find stellar-mass fractions of 50-100% within the Einstein radius[45]). For the NE galaxy, we find an Einstein radius of 0.05″, while for the SE galaxy we find an Einstein radius of 0.03″. As the separation between these sources and z8_GND_5296 is ~2.3″ and 3.2″, respectively. Additionally, even the largest Einstein radius from the strong-lensing galaxies of Sloan Lens ACS Survey[45] would reach only 1.3″ at $z = 0.39$ (for a lensing galaxy with stellar mass $>10^{11}$ M$_\odot$; more than 100 times that of the $z = 0.39$ galaxies here).. We thus conclude that strong gravitational lensing is not affecting the inferred luminosity.

4.4 Spectral Energy Distribution Fitting In the above subsections, we have attempted to discern between the [O II] and Lyα identification of the detected emission line by looking at the line properties itself. However, the strongest evidence either way can likely be had by looking at the full photometric SED. Although an emission line near a spectral break can be indicative of both Lyα or [O II], the stellar populations which would create these signatures would be drastically different. We utilized the same *HST* photometry that went into the photometric redshift fitting, only now we also added in *Spitzer*/IRAC data at 3.6 and 4.5μm. We utilized new IRAC data from the *Spitzer* Very Deep Survey of the HST/CANDELS fields (S-CANDELS; PI Fazio), which is a Cycle 8 *Spitzer*/IRAC program to cover the CANDELS wide fields (0.2 deg^2) with a total integration time of ~50 hr in both IRAC bands at 3.6 and 4.5 μm. S-CANDELS data acquisition in the CANDELS GOODS-N field was completed over the course of two visits, during 2012 January and 2012 July. The data were reduced to mosaic form following procedures identical to those described for the coextensive, wider but shallower *Spitzer* Extended Deep Survey.[46] At the position of z8_GND_5296, the exact integration times are 47.2 and 57.8 hr in the 3.6 and 4.5 μm bands, respectively. A rms image was produced for each band by taking the inverse of the square root of the coverage map, and scaling it so that the mean value was equal to the mean of the pixel-to-pixel fluctuations in empty regions of the image.

As shown in Figure S3, z8_GND_5296 is clearly detected in both bands, but due to the large beam of *Spitzer*/IRAC, simple aperture photometry will result in inaccurate fluxes due to contamination from nearby neighbors. We therefore fit and subtracted nearby sources in a 19″ × 19″ region around z8_GND_5296 in each of the IRAC images. Positions, magnitudes, and radial profiles of the sources in this region were derived by running Source Extractor on the higher

Table S2: Measured Broadband Flux Densities of z8_GND_5296

F435W	F606W	F775W	F814W	F850LP	F105W	F125W	F160W	3.6μm	4.5μm
-5.4 ± 10.5	-5.0 ± 8.5	17.8 ± 13.9	0.0 ± 5.04	0.7 ± 16.0	102 ± 10	194 ± 12	218 ± 14	256 ± 25	631 ± 51

Table S2 | All fluxes are in nJy (10^{-32} erg s^{-1} cm^{-2} Hz^{-1}). While the measured signal-to-noise in the F775W band is 1.3, the lack of detections in all other optical bands (including the stacked optical image) as well as in a smaller circular aperture implies that this is due to random noise.

Table S3: 68% Confidence Range of Physical Properties for z8_GND_5296

z	Stellar Mass (M$_\odot$)	Age (Myr)	E(B-V)	SFR (t < 10 Myr) M$_\odot$ yr^{-1}	EW ([O III]) (Å)
7.51	$0.9 - 1.2 \times 10^9$	$1 - 3$	$0.12 - 0.18$	$320 - 1040$	$560 - 640$
1.78	$1.6 - 1.8 \times 10^9$	$510 - 570$	$0.0 - 0.0$	$0 - 0$	—

Table S3 | The values given correspond to the 68% confidence range for the quoted parameters. The initial mass function (IMF) was assumed to be Salpeter; were it of a Chabrier form, the stellar masses and star-formation rates would be lower by a factor of 1.8.

resolution *HST* F160W-band images. Each source found, including z8_GND_5296, was modeled on the IRAC images with the galaxy-fitting software package GALFIT[47] (v3.0) in a manner similar to our previous work.[48] Figure S3 illustrates the process. GALFIT requires a point-spread function (PSF), which was constructed using stars in the large IRAC mosaics. The FWHMs of the IRAC PSFs were 1.9″. The extracted AB magnitudes of z8_GND_5296 are $m_{3.6} = 25.38 \pm 0.09$ and $m_{4.5} = 24.40 \pm 0.07$. We note that these photometric errors include the uncertainty due to deblending, which we verified by varying the neighbor fluxes within their 1σ uncertainties, and noted that it changed the flux of the galaxy of interest by $\leq 9\%$ for the 3.6 μm band, and $\leq 5\%$ for the 4.5 μm band; both at or less than the quoted photometric uncertainties. As expected from inspecting the image, the 4.5 μm flux is much brighter, which we will comment on below. We also included constraints during SED fitting at 5.8 and 8.0 μm, using images from the GOODS *Spitzer* survey. There was no significant flux at the position of z8_GND_5296 (as expected for a source at high redshift), thus during the SED fitting, these fluxes were set to zero, and the flux errors were set to the 1σ limit of the images, which are 23.485 for 5.8 μm and 23.355 for 8.0 μm. These limits are 1-2 mag brighter than both of our best-fit models. The photometry of z8_GND_5292 is listed in Table S2.

We compared the 12 photometric points of our SED to a suite of stellar population models, using the updated models of Bruzual & Charlot.[49] In these models, we assumed a Salpeter initial mass function, and varied the stellar population age, metallicity, dust content and star-formation history. There is mounting evidence that a dust attenuation law, $A(\lambda)/E(B - V)$, similar to that derived for the Small Magellanic Cloud (SMC) better reproduces the UV-optical colors and IR/UV ratios for young, presumably lower-metallicity galaxies at high redshifts,[50–52] compared to the dust attenuation law for local UV-luminous starbursts[53] that is more commonly used (see discussion in Tilvi et al.[51]). This is perhaps unsurprising as the SMC is frequently pointed to as a local analog for high-redshift galaxies. We thus use the SMC dust-attenuation curve derived by Pei[54] to model the effects of dust on our model spectra. Additionally, recent evidence implies that high-redshift galaxies likely have a rising star-formation history on average,[50,55–57] thus we allow both exponentially rising and declining star-formation histories. The stellar mass is found as the normalization between the observed fluxes and the best-fit model. We include nebular emission lines using the emission line ratios published by Inoue et al. (see also Salmon et al., in prep).[58] The best-fitting model is found via χ^2 minimization, and the uncertainties on the best-fitting parameters are found via Monte Carlo simulations, varying the observed fluxes by an amount proportional to their photometric errors. This procedure is

similar to that used in our previous work, to which we refer the reader for more details.[15,20]

We perform two fits; first fixing the redshift to $z = 7.51$ should our detected line be Lyα, and secondly fixing $z = 1.78$, if the line were [O II]. We note that in the high-redshift fit, we exclude the Y-band photometry, as the highly-star-forming nature of this object implies that it likely has strong intrinsic Lyα emission, which will be included in the models. However, given the weak Lyα flux observed, the emission is likely being attenuated by gas somewhere along the line-of-sight; this effect is not included in the modeling. As briefly discussed in the main text, the observed photometry of this source is much more consistent with a redshift of 7.51, and thus a line identification of Lyα (reduced $\chi_r^2[z = 7.51] = 0.8$ and $\chi_r^2[z = 1.78] = 14.7$). This is primarily due to two wavelength regimes, highlighted by the right panel of Figure 3, which shows the values of χ^2 for each band and redshift. First, z8_GND_5296 is completely undetected in the optical, even when stacking the two redder bands. As can be seen in Figure 3, the lack of a significant detection in these bands strongly favors the high-redshift solution, with $\Delta\chi^2$ ($\chi_{z=1.78}^2 - \chi_{z=7.51}^2$) = 2.0, 17.6 and 3.4 for the F606W, (ultradeep) F814W and F850LP bands, respectively (the F775W band is less discerning, as it has a formal 1.3σ detection; due to the non-detections in the surrounding bands and in the stack of all optical bands, as well as the non-detection in this band in a smaller circular aperture, we attribute this to random noise). Second, the IRAC bands also strongly favor the high-redshift solution, with $\Delta\chi^2 = 19.1$ and 17.4 for the 3.6 and 4.5μm bands, respectively. This is understandable as at $z = 7.5$, [O III] is located in the 4.5 μm band, and a strong emission line could create the observed color. At $z = 1.78$, there is no such strong emission line in this band, thus the models struggle to fit the observed color. As we discussed in the main text, the inferred [O III] EW can be used to diagnose the metallicity of this galaxy. We quote the [O III] EW as that from the best-fitting model, with the quoted 68 and 95% confidence ranges coming from the Monte Carlo simulations.

The SFR quoted in Table S3 is a time averaged SFR. For models where the stellar population age is older than 100 Myr, we integrate the star-formation history over the past 100 Myr to determine the SFR. For younger populations, we simply divide the stellar mass by the stellar population age. This time-averaged SFR is extremely high for our $z = 7.51$ fit, with a 68% confidence range from $320 - 1040$ M$_\odot$ yr^{-1} (best-fit = 330 M$_\odot$ yr^{-1}). Given the observed photometry, this is plausible, as the bright rest-frame UV coupled with strong inferred [O III] emission drives the fit to a young age (3 Myr in this case), when the SFR will be very high. However, any SED-fitting-based SFR for very young ages will be extremely sensitive to very short timescale variations in the SFR that are extremely difficult to constrain, thus the inferred SFR has

a large uncertainty. Although a young age is necessary to reproduce the inferred [O III] EW, metallicity will also have a strong effect on the [O III] EW, and we only coarsely sample the metallicity. To see what constraints we can place on the SFR without requiring assumptions on the [O III] line, we performed another fit to the data, excluding the IRAC 4.5 μm band. In this fit, the time-averaged SFR ranges from $120 - 530$ M$_\odot$ yr^{-1} (best-fit = 260 M$_\odot$ yr^{-1}). Thus, even without allowing the [O III] emission to influence our fit, this galaxy still has an extremely high time-averaged SFR.

As one final check, we calculate the SFR using the UV-luminosity to SFR conversion published by Kennicutt et al.,[59] which provides a SFR 68% confidence range of 50–90 M$_\odot$ yr^{-1}, significantly lower than the range derived from our SED modeling. However, this UV-to-SFR conversion assumes constant star-formation over the previous 100 Myr,[59] whereas our analysis favors substantially younger stellar populations. Therefore, this conversion will significantly understate the SFR in such galaxies (and caution should be used when interpreting the SFRs inferred from the UV luminosity that do not correct for possibly low ages[9,60]). In the main text, we thus assume the fiducial SFR of 330 M$_\odot$ yr^{-1}, with the caveat here that given uncertainties in modeling the [O III] emission, it may be slightly lower. In the main text, we discuss the implications of such a high SFR, assuming that it is due to fueling via gas accretion from the IGM. Alternatively, this high SFR could be due to a merger-induced starburst, which would be detected at its peak SFR with a $\sim 10-20\%$ probability [61]. This galaxy does appear to have a faint companion, though a clumpy morphology is not necessarily indicative of an ongoing merger[62].

As noted in the main text, the best-fit model for the low-redshift solution has zero [O II] emission line flux, inconsistent with the spectroscopic detection of our emission line, providing further evidence for our high-redshift solution. To see if we could reconcile the photometric non-detection at < 1 μm with the detectable emission line flux if the line were [O II], we tried fitting this galaxy with two populations – one maximally old (formed at $z = 20$), and one with an age and star-formation history which was allowed to vary. Even including the emission line flux as a constraint, this fit still preferred a completely passively evolving model with minimal line emission.

[O II] emission at $z = 1.78$ could be consistent with a passive population if the galaxy hosted an active galactic nucleus (AGN). This is unlikely as there is no *Chandra* X-ray source within $30''$. [63] The *Chandra* imaging reaches $L_x = 10^{42}$ erg s^{-1} at $z = 1.78$, sufficient to detect weak AGNs. Additionally, there is no counterpart at $\lambda > 24\mu$m in *Spitzer*/MIPS, *Herschel*/PACS or SPIRE or JVLA data.[?,?] To determine whether these data can exclude obscured AGNs, we compared several template obscured AGN to both our *Hubble* and *Spitzer*/IRAC observations, as well as these longer wavelength limits. **MAKE PLOT**

For the high-redshift solution, as shown in Figure 3 the model fitting prefers strong Lyα emission. The best-fit model has a Lyα line flux of 4.2×10^{-17} erg s^{-1} cm^{-2}, or a factor of $\sim$15 greater than our observed line flux (likewise, the best-fit model rest-frame Lyα EW is 120 Å). This is certainly due to the way we treat Lyα in our modeling, where we follow our previous work[13,64] and assume that half of the line is subject to the IGM optical depth at 1215Å. This is analogous to a Gaussian line symmetric about the resonance wavelength of Lyα. However, as discussed above, this is rarely the case; in fact, Lyα is typically observed to be redward of the systemic redshift due to radiative transfer effects. However, in these cases, all of the line flux blueward of 1216 Å as well as many of the photons redward of resonance (due to the damping wing) are scattered by neutral hydrogen. Thus, the observed line flux may be severely attenuated from the intrinsic line flux.[42,65] As our stellar population model implies significant star-formation, its not surprising that this galaxy may indeed have a very strong line flux. The factor of $\sim$15 difference between the best-fit
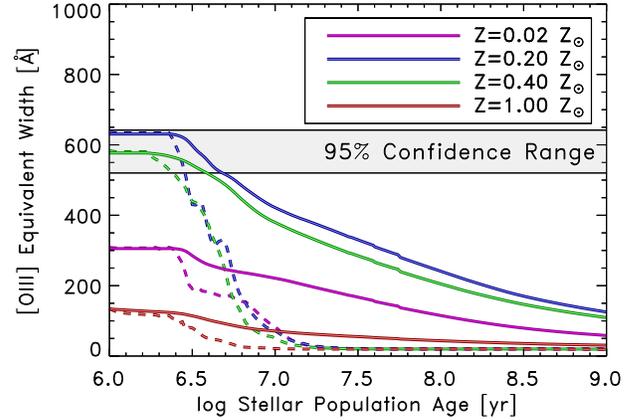
Figure S4 | **[O III] EW variation with age and metallicity**. The change of the rest-frame [O III] λ5007 EW with stellar population age, for the considered values of metallicity. The solid lines represent a continuous star-formation history, while the dashed lines represent an instantaneous burst. The 95% (2σ) confidence range of our inferred [O III] EW, 520–640 Å, is denoted by the gray bar. At 95% confidence, we can restrict the gas-phase metallicity in this galaxy to be sub-solar yet $>0.02Z_\odot$. These results are consistent with the stellar metallicity results from the SED fitting; which also prefer $Z = 0.2$–0.4 $Z_\odot$.

line flux and our observed Lyα line flux could further imply that the Lyα flux of this galaxy is being severely attenuated, perhaps due to a rising neutral fraction in the IGM (see the following section).

4.5 [O III] Emission Though typically the small variations of galaxy SEDs with changing metallicity makes conclusions on the metallicity difficult from photometry alone, the strong inferred [O III] emission in our object makes at least moderate conclusions possible. In the main text we discussed how the strong [O III] emission can be used to constrain the metallicity of this galaxy. Figure S4 shows how the [O III] EW varies with age as a function of stellar population metallicity. Unfortunately, as we are limited to the metallicity grid of our chosen stellar population models (which are not unlike most available models), we cannot make a precise determination of the limits of the metallicity in this galaxy. However, as shown in Figure S4, we can make a few conclusions. First, models with solar metallicity cannot come within a factor of three of creating such high [O III] emission, thus even one of the highest-star-forming galaxies in the distant universe cannot enrich to $\sim$Solar metallicity by $z \sim 7.5$. Secondly, even with a continuous star-formation history, models with $Z = 0.02$ $Z_\odot$ are still excluded at $\gg$95% confidence. Models with 20 or 40% Solar metallicity can reproduce our inferred [O III] EW, though with relatively young ages, consistent with the results from our SED fitting. Additionally, we also have constraints on the stellar metallicity from our SED fitting, as we found that all of our 1000 Monte Carlo simulations preferred a metallicity of either 0.2 or 0.4 $Z_\odot$. The conservative conclusion from these two results is that $0.02 < Z/Z_\odot < 1.0$ at very high confidence, and given the metallicity spacing of our model grid, $0.2 < Z/Z_\odot < 0.4$ is in good agreement with our measurements. Further nebular modeling may yield a more precise lower limit for the metallicity in this system, but the best results will come from rest-frame optical nebular line spectroscopy with the *James Webb Space Telescope*.

5 EW Evolution

Here we examine the implications of our lone emission line detection. We performed a simulation to predict the number of galaxies we would expect to observe using a fiducial Lyα EW distribution, with the goal of measuring the significance at which we could rule out a given distribution. For these simulations, we included all high-redshift candidate galaxies observed on both masks. We chose as our EW distribution the predicted $z = 7$ Lyα EW distribution from Stark et al.[18]
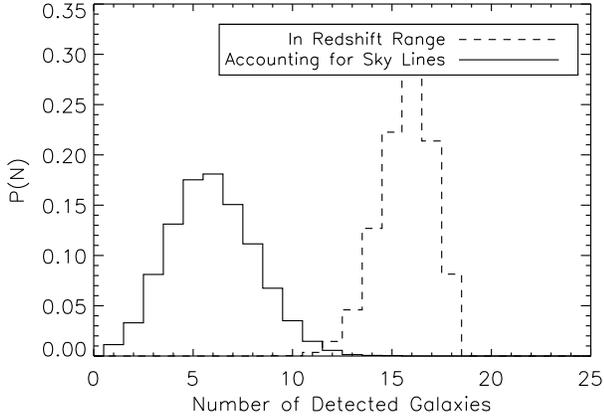
Figure S5 | EW test. The results of our Lyα EW evolution test, assuming that the Lyα EW distribution at $z = 7$ continues its upward evolution with redshift observed at $z = 3 - 6$. The dashed curve shows the expected number of detected galaxies in our MOSFIRE data accounting for only the spectral range observed. The solid line shows how this changes if we also assume that we will not detect lines which fall on a night sky emission line; these sky lines reduce the expected detected number by >50%. Even accounting for this, our simulations show that if the EW continues its evolution previously observed at $z = 3$–6 out to $z = 7$, we would have expected to detect Lyα at >5σ significance from 6 galaxies. The fact that we only detected one such source implies that the Lyα EW distribution has evolved at 2.5σ significance.

They use observations of the evolution of the Lyα EW distribution at $3 < z < 6$ to predict what the distribution would be at $z = 7$, assuming the IGM state is unchanged. We approximate this distribution as a constant probability from 0 Å $< $ EW < 40Å then falling off at EW > 40Å as a Gaussian centered at 40Å and with FWHM = 60Å. We assigned EWs to our galaxies with a Monte Carlo approach, in each simulation randomly drawing an EW from the predicted distribution, and then computing the corresponding Lyα line flux using the continuum flux of the given galaxy redward of the line. In each simulation for each observed candidate galaxy, we first drew a redshift from the galaxy's redshift probability distribution function. If the corresponding Lyα wavelength fell outside the MOSFIRE Y-band spectral range, or if it fell on a sky emission line (using an extracted sky spectrum to denote the position and extent of emission lines), then the galaxy was marked as not detectable. For all galaxies in a given simulation which would have Lyα falling in a clean region of the MOSFIRE Y-band, we then compared the simulated Lyα line flux to the 5σ limit of our observations. If the line flux was above this value, the candidate galaxy was marked as detected, otherwise it was left undetected.

For the 5σ line flux, we tried two different values. First, we assumed our predicted spectroscopic depth of 2.1×10^{-18} erg s^{-1} cm^{-2} (5σ), from the MOSFIRE exposure time calculator (this is the value that was used in the main text). As shown in Figure S5, this simulation predicts that we should have detected 6.0 ± 2.2 galaxies. Out of the 10^4 simulations run, in only 113 simulations was one or zero galaxies detected at $\geq 5\sigma$, thus we can rule out this EW distribution at 2.5σ significance. We note that the consideration of the sky emission lines plays a key role, as ignoring their presence would have led us to believe that we should have detected about 10 more galaxies. As a second test, we used our flux-calibrated emission line flux of 2.64×10^{-18} erg s^{-1} cm^{-2}, at 7.8σ significance, to compute an empirically-derived 5σ sensitivity of 1.7×10^{-18} erg s^{-1} cm^{-2}. With this as the limit for detection, we find that this EW distribution would have predicted 6.0 ± 2.2 galaxies to be detected; in this scenario, this EW distribution can be ruled out at 2.6σ significance. Given the modest uncertainties inherent in our flux calibration, we consider the first scenario a more conservative result, though the results are very similar (primarily because the

assumed EW distribution yields predicted line fluxes for most galaxies brighter than either flux limit). We will consider the lack of detected emission lines in more detail in a followup paper.